3-Φ Coupled Inductors Design and Characterisation with Calorimetric Apparatus

Johan LE LESLÉ♠, Guillaume LEFEVRE♠, Samuel SIEDEL♣
♠Mitsubishi Electric R&D Centre Europe, Rennes, France
♣Univ. Grenoble Alpes, CNRS, Grenoble INP, SIMAP, Grenoble, France

RESUME – This paper presents the design and the experimental characterisation of a Printed Circuit Board (PCB) based three-phase coupled inductors. The prototype is meant to be implemented in an interleaved buck converter (IBC). The main objective is to push the efficiency and power density forward compared to more conventional PCB planar un-coupled inductors. The results of the optimisation procedure combining Finite Element Analysis (FEA) and analytical study are analysed. This paper also describes the practical implementation with the corresponding PCB layout and stack-up. Then, the results of the experimental characterisation, including losses measurement using a flow-calorimeter set-up are also presented.

Mots-clés – Optimisation, Coupled Inductors, PCB Integration, Calorimetric Measurements.

1. INTRODUCTION

The expansions of E-mobility and the More Electric Aircraft (MEA) concept are pushing towards higher efficiency and higher power density power converters, increasing the adoption of Wide Band Gap (WBG) devices thanks to their higher performances. Nevertheless, the conventional wire bonded packaging does not allow to get the most out of WBG because of the high stray inductance. To overcome this packaging issue, one of the best candidates among new concepts is the PCB embedding where the power dies are directly placed within the PCB substrate [1]. This low-cost process proposes effective solutions for short electrical interconnections, improved thermal management and higher power density. Besides, modular design approach and elementary cells interconnection also help reaching the objectives owing to interleaving and increased apparent frequency. Despite performance improvements and size reduction brought by PCB-embedded WBG and modular design, a breakthrough is only possible if magnetic components are simultaneously enhanced. The work presented in this paper is a salient point for the improvement of the Power Building Block (PBB) introduced in [2]. This PBB is made of three parts, the power stage located in the central part, the gate driver on one side, and the filtering inductor on the other side. The 100 kW DC/DC converter is made of six PBBs assembled side-by-side, with the set of specifications presented in the Table 1. Looking at the overall converter, the magnetic components represent almost 80 % of the overall volume. The initial design suffered by two aspects. First, the inductor's volume was mainly dictated by the DC magnetisation, and secondly, the Soft Magnetic Compound (SMC) implemented as the magnetic core exhibited excessive losses [3]. Operate at lower AC induction field could have been possible by increasing the number of turns (N_T) but, since lower permeabilities were hard to reach with good repeatability with the SMC, saturation may have occurred due to the higher DC field component. To tackle this issue, the most intuitive countermeasure is to change the magnetic material for reducing core losses. Unfortunately, among the conventional low permeability (μ) materials [4, 5], no relevant alternative was identified when considering the permeability versus losses trade-off. As discussed in [6] with N87 ferrites, loss-optimal inductor designs are significantly capped by the DC induction field, especially when increasing the switching frequency (f_{SW}). To mitigate the impact of the DC magnetic field and further improve the filtering inductor, the selected option was to investigate inverse magnetic coupling. This design technique offers several advantages, such as reduced volume and losses [7, 8, 9]. Also, for high coupling factors, two side-effects of more symmetric operations over the (B,H) quadrants are:

Table 1. Electrical specifications of single PPB being part of the 100 kW DC/DC Converter

$V_{DC\ max}$ [V]	$I_{DC/\Phi}$ [A]	fsw [kHz]
700	55	150

1. A reduced impact of DC pre-magnetisation allows to reduce core losses.
2. A reduced DC bias impact on permeability leading to higher magnetising inductance, and consequently reduced AC copper losses.

For volume constrained applications (automotive, aircraft, datacenters) or fast response time, the concept of coupled inductors has been widely used for years [10, 11, 12]. Due to symmetry and simple implementation based on off-the-shelf cores, the preferred option is dual coupled chokes. Although possible, and offering outstanding performances, the monolithic extension to an arbitrary number of phases (N_Φ) remains marginal in the literature. Optimal performances being obtained with symmetric coupling coefficients (K), this solution ideally requires bespoke cores or special winding arrangements [13, 14, 15, 16]. Hence, for multiphase systems with $N_\Phi > 2$, it is common to consider cascaded structures with sets of dual coupled inductors [7, 9, 15, 17]. In such a case, the resulting current at twice the input frequency is not filtered out with the leakage inductance (L_{Lk}) but throughout the magnetizing inductance (L_M) of the following inductive stage. Nonetheless, a dedicated inductor is necessary to filter out the output current at $N_\Phi.f_{SW}$, but the design constraints are drastically alleviated.

For kW scaled converters, PCB based coupled inductors are widespread, in particular for interleaved PFC rectifiers operating in the MHz range. This solution basically offers the potential for repeatability and automated manufacturing of a single board for active and passives. Even so, when implemented in tens of kW

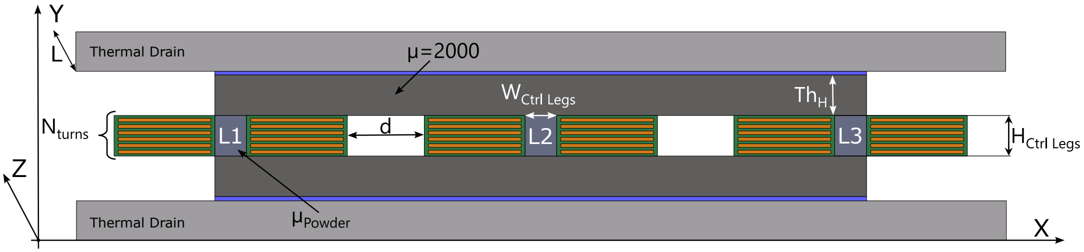

Figure 1. Illustration of the cross-section of the investigated coupled inductor concept

power systems, coupled chokes are generally wound with plain wires, Litz wires or foils to minimize DC and AC copper losses [18, 7, 9]. However, in [19], a coupled inductor concept based on PCB technology was proposed for a 22 kW on-board charger. A similar approach was considered for coupled inductors dedicated to a 50 kW DC/DC converter in [20], requiring 500 µm thick copper layers.

In this paper, the design procedure for a 50 kW power rated coupled magnetic component and the corresponding outcomes are presented. Then, the practical implementation of the selected design based on thick copper PCB, and the experimental characterisations are discussed. In addition, the loss measurement set-up, being a back-to-back converter coupled to a flow calorimeter is presented. The practical implementation of the calorimeter, and the associated calibration procedure required for accurate results are detailed.

2. COUPLED INDUCTORS DESIGN

As mentioned, the investigated magnetic component is meant to be implemented into a 100 kW 6-Φ highly integrated IBC. Multicellular power converters have the advantages of complying with several types of application with different power ratings, or for improving the efficiency over the full power range through cell shading. For this project, the minimal targeted power was 50 kW, thus the number of phases has been settled to three. The geometrical variables are limited by the mechanical constraints coming from the PBB, and the side-by-side assembly. In fact, the overall width of the magnetic components is settled to comply with the former power module assembly. The Figure 1 is illustrating the concept of the PCB based coupled magnetic components using low and high permeability materials for the vertical and horizontal blocks, respectively iron powder and ferrite. The vertical magnetic block is defining the magnetising inductance for each phase and the coupling factor between the phases in combination with distance (d) between them. Indeed, a low vertical reluctance (higher µ and larger magnetic cross section (Ae)) associated to very close windings would lead to high coupling coefficient. Ferrite materials have been preferred for the horizontal magnetic block to ensure magnetic short-circuit mitigating the asymmetrical behaviour, and to maintain low magnetic core losses. Nonetheless, the ferrite block will cap the power density because of its lower saturation level (~500 mT at 25°C). Hence, the ferrite thickness (Th_H) is selected according to off-the-shelf cores having the highest value (6 mm). Based on these constraints, the optimisation variables are the permeability and the width of the vertical magnetic block material, μ_{Powder} and $W_{Ctrl\ Legs}$, respectively. As the overall width of the system is settled, the wider $W_{Ctrl\ Legs}$, the lower "d". The number of turns depends on the PCB stack-up, to ease the PCB design, only one turn per layer is assumed. Thus, N_T is limited to even values capped by the overall PCB thickness manufacturing capabilities. The number of turns also defines the height of the vertical magnetic block ($H_{Ctrl\ Legs}$). The length of the device L (in the Z axis) is the only lever to increase the power density, therefore the shortest device is targeted.

2.1. *Design Procedure*

The developed design procedure is combining automatically generated 2D FEA and analytical study by coupling FEMM to Matlab, the overall optimisation flowchart being presented in the Figure 2. The FEA part allows to get the linear inductance values (self-inductance (L_M) and mutual inductances (M)); so the coupling factors (K) between the three inductors, and the DC + AC winding's resistances (R_{DC} & R_{AC}) based on a harmonic study, still per unit length. The inductance matrix [L_{Mat}] is easily obtained by imposing a current, either DC or AC, into a winding and looking at the useful flux or the induced voltage across the other phases, respectively. The number of simulations depends on the number of phase being equal to N_Φ-1 for all the investigated frequency harmonics (H_n). The R_{AC} depends on the current allocation into the winding being impacted by "K" acting on the magnetic field within the winding window. Therefore, a frequency dependant current vector is first calculated according to L_{Mat}, and a defined voltage vector. The calculated currents are then imposed to the respective windings to get the R_{AC} at the corresponding harmonic.

Those results, (L_{Mat}, $R_{DC\ Lin}$& $R_{AC\ Lin}$) feed the Matlab routine to calculate losses, and magnetic field under nominal operation conditions. The optimisation procedure allows to quickly analyse the results and get the best trade-off between the losses and the volume (∝ to L). The AC copper losses ($P_{Cu_{AC}}$) calculation requires to define the current waveforms based on the voltage applied to the inductors - being function of the DC bus voltage (V_{DC}), the duty cycle (α), the phase-shift between the phases ($\varphi = \frac{2\pi}{N_\Phi}$) - and also depending on [L_{Mat}]. Therefore, the HF inductor currents are calculated according to the Fourier's expansion of the square shaped voltage vector. Then, the AC copper losses are simply calculated with the R_{AC} extracted from the FEA at the corresponding harmonic.

The next step in the optimisation procedure consists in calculating the induction within the magnetic cores; the maximal induction value being defined by the ferrites, with a saturation close to 400 mT at 125 °C. Another critical point which cannot be avoided is the impact of DC current mismatches on the DC induction. In such a system, current balancing control loop is a must to mitigate the phase currents unbalances. Nevertheless, some can remain because of discrepancies in the individual current measurement chains, or even because of common mode noise. To illustrate the thought, FEAs have been conducted with an eight-turns, 100 mm long device and 50 A ± ε DC currents, with ε = ± 3 %, being also the value set into the optimisation procedure. The results are presented in the Figure 3. Under balanced conditions, the average flux density in the left-hand side of the ferrite is approximately 140 mT while under unbalanced conditions the flux density is 220 mT, being 1.6 time higher. Under unbalanced conditions, the current difference is magnetising the device through L_M (high value) instead of L_{Lk} (low value),

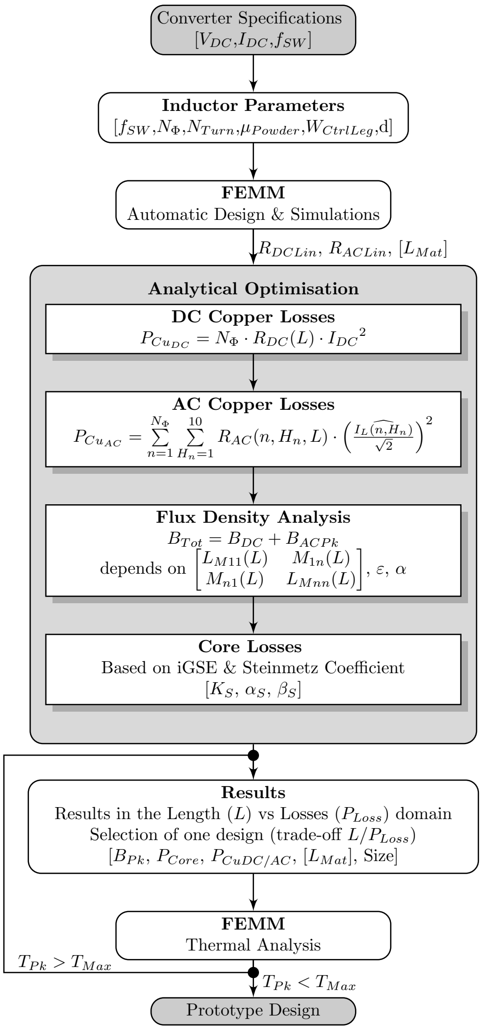

Figure 2. Coupled inductor optimisation flowchart

this phenomena has a very strong impact on the size reduction. In the optimisation procedure the worst case is considered, which is an excess of current within one of the external winding, see equation 1.

$$\begin{bmatrix} B_{DC1} \\ B_{DC2} \\ B_{DC3} \end{bmatrix} = \frac{L}{N_T(LTh_H)} [L_{Mat}] \, I_{DC} \begin{bmatrix} 1+\varepsilon \\ 1-\varepsilon/2 \\ 1-\varepsilon/2 \end{bmatrix} \tag{1}$$

The AC induction is calculated based on Faraday's law considering the critical conditions, being the maximal voltage-time product ($V \times t$), at the highest DC bus voltage and for $\alpha = 0.5$, and still considering the ferrite's dimensions, see the equation 2. The peak flux density (B_{Pk}) is then the sum of B_{DC} and $B_{AC\,Pk}$.

$$B_{AC\,Pk} = \frac{V_{DC}}{8 N_T f_{SW} Ae(L)} \tag{2}$$

To complete the study, the core losses are calculated. In this procedure, the Steinmetz coefficient of the different materials are used in the improved Generalised Steinmetz Equation (iGSE), being well documented in the literature [21].

2.2. *Optimisation Results*

This section analyses the optimisation results and highlights the impact of the variables presented in the Table 2. The results are only considering vertical magnetic blocks made of iron powder, having a permeability of 26. In fact, using a higher μ material is limiting the size reduction because of higher B_{DC} induced by higher L_M along with current mismatch .

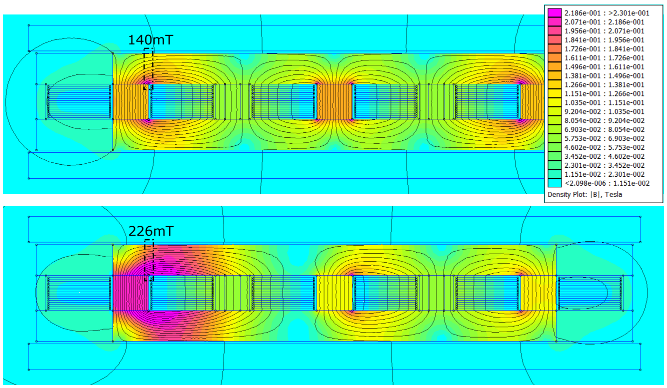

Figure 3. FEA results highlighting the impact of unbalanced DC currents ($\varepsilon = 3\,\%$) in the coupled inductors. (Top) FEA results with balanced currents, $I_{DC1} = I_{DC2} = I_{DC3} = 50$ A. (Bot) FEA results with unbalanced currents, $I_{DC1} = 51.5$ A & $I_{DC2} = I_{DC3} = 49.25$ A.

Table 2. Optimisation variables defining the design space

Variables	Range	Comments
μ_{Powder}	26	Limited by materials (BK14060A026)
$W_{Ctrl\ Legs\ [mm]}$	$[4 \dots 8; 1]$	Arbitrarily defined
N_T	$[4 \dots 8; 2]$	Dictated by PCB Process
L [mm]	$[48 \dots 143; 9.5]$	Init. inductor length 143 mm

The Figure 4 is depicting the impact of the optimisation variables (N_T, $W_{Ctrl\ Legs}$ and L) on the losses. As the target is the best trade-off losses versus length, only the impact of the two other variables will be analysed. Looking at the impact of N_T first, referring to the markers in the legend. More turns is beneficial for the core losses since the peak-to-peak induction swing (ΔB) is inversely proportional to N_T. However, the impact of N_T on the copper losses is less obvious because of the combination of DC and AC losses. The increase in N_T definitely leads to higher winding resistance, but also inductances (L_M and L_{Lk}), thus the current ripple is reduced, mitigating the AC copper losses at f_{SW} and $N_\Phi . f_{SW}$. Similarly, the change in N_T impacts in opposite directions DC and AC inductions, the B_{DC} will increase proportionally to N_T while B_{AC} will decrease, see the Figure 5

The other variable, $W_{Ctrl\ Legs}$, has a smaller impact on the induction, but the increase in $W_{Ctrl\ Legs}$ intends to increase B_{Pk}.

Table 3. Details about the selected design from the optimisation procedure

$\mu_{Powder} = 26$	$P_{Tot} = 132$ W
$N_T = 8$	$P_{Cu\,DC} = 21$ W/Φ
$W_{Ctrl\ Legs} = 7$ mm	$P_{Cu\,AC} = 15$ W/Φ
$L = 90$ mm	$P_{Iron} = 5$ W/Φ
$B_{DC} = 245$ mT	$P_{Ferrites} = 8.4$ W
$B_{AC} = 130$ mT	
$L_{Mat} = \begin{bmatrix} 134 & -67 & -54 \\ -67 & 146 & -67 \\ -54 & -67 & 134 \end{bmatrix}$ μH	

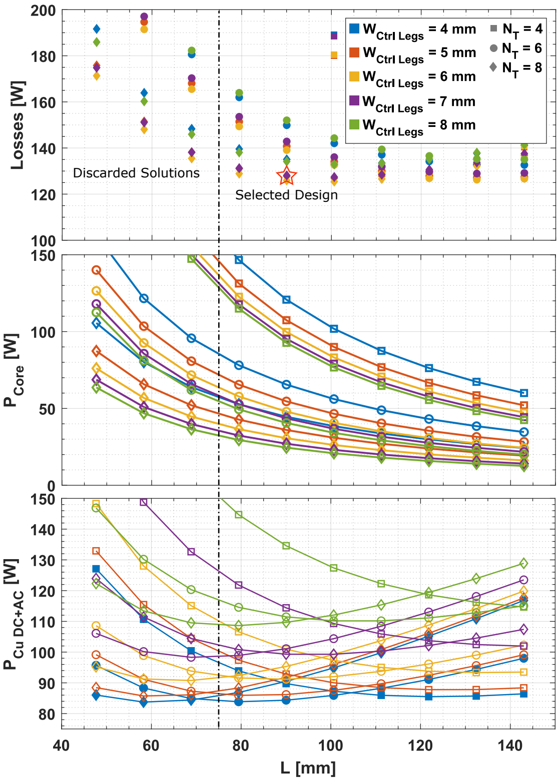

Figure 4. Analysis of the impact of N_T and $W_{Ctrl\ Legs}$ on the losses with $\mu_{Powder} = 26$.

In fact, higher $W_{Ctrl\ Legs}$ leads to a lower distance between the phases, reducing L_{Lk} and increasing L_M, so a higher B_{DC}. Looking at the losses, this variable impacts copper and core losses. Starting with the core losses, an increase in the vertical block Ae allows decreasing ΔB, so the corresponding losses. However, the $N_\Phi.f_{SW}$ current ripple, being a major contributor to the AC copper losses, increases due to lower L_{Lk}.

Finally, the selected design has $N_T = 8$ and $W_{Ctrl\ Legs} = 7$ mm. The overall details on the selected design are presented in the Table 3. It is important to note that for a perfectly symmetrical 3-phases design, the phase-to-phase coupling coefficient cannot exceed 50 %. Despite the asymmetrical design, good coupling coefficients can still be obtained. The central-to-side coupling coefficients are $K_{21} = K_{23} = 48$ %, while the side-to-side coupling coefficient is reduced to $K_{13} = 40$ %. Thus, 88 % of the DC induction can be cancelled (in the case of perfectly balanced DC Current operation). Having good magnetic coupling is the key stone for size reduction, the selected design being 40 % shorter than the former single phase design, with only 134 W power losses for the complete 3-Φ system.

2.3. *Prototype Manufacturing*

The selected design requires an eight 400 µm thick copper layers PCB. Maximal standard PCB thickness is usually 3.2 mm, being already the overall thickness of only the copper layers. Thus, the full board thickness must be in the range of 4 mm to 5 mm. Only few PCB manufacturers have the capabilities to produce such a thick PCB with thick copper layers. For this project, the PCB has been manufactured by Serigroup PCB. Their capabilities allowed, to not merely reach the targeted PCB thickness, but also to use buried and blind vias facilitating the layout design and the turn-to-turn interconnections. The final prototype is presented in the Figure 6. The vertical magnetic blocks are machined in house from High Flux magnetic blocks and the top/bottom ferrites are made with N95 plates

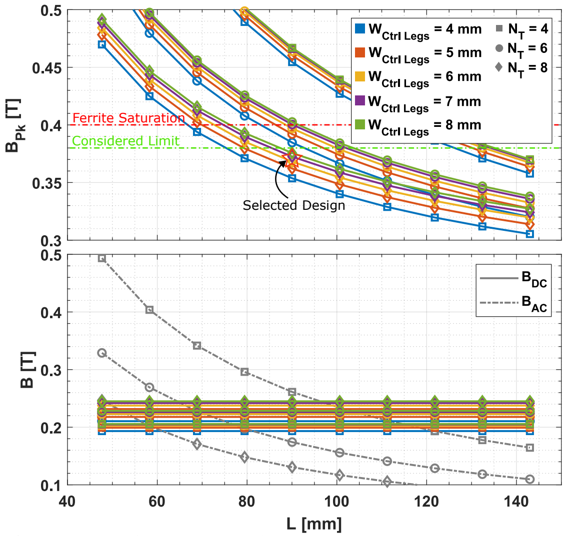

Figure 5. Analysis of the impact of N_T and $W_{Ctrl\ Legs}$ on the induction with $\mu_{Powder} = 26$.

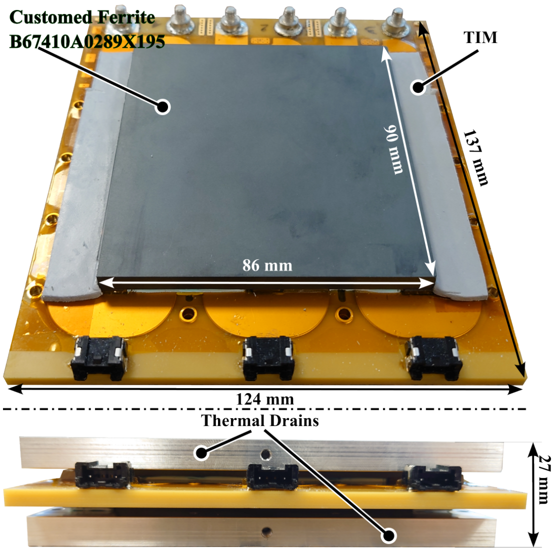

Figure 6. Prototype of the 3-Φ coupled inductors and their thermal drains

(B67410A0289X195) also customised in house. Height mismatches, added to inherent parasitic air gaps coming from the assembly, induce some variations of the inductance values.

3. EXPERIMENTAL CHARACTERISATION

Experimental characterisations have been conducted on the prototype to validate the theoretical design (electrical, magnetic and thermal). The small signal characterisation allowed to validate L_M and K. The deviation between the measurements and the theoretical value is about 20 %, mainly coming from residual, and inevitable, air gaps. The results are summed-up into the Table 4. Then, the saturation behaviour of the system has been investigated through double pulse test (DPT) to define the maximal voltage.time (V×t) product, and also under continuous operation conditions under reduced DC voltage and switching frequency. The second protocol allows to consider the DC current unbalances coming from the test-bench. Finally, the prototype's losses have been measured under nominal operation conditions (V_{DC}, f_{SW}, etc) using a back-to-back converter associated to a steady-flow calorimeter, being further detailed hereafter.

Table 4. Inductance and coupling matrix obtained with impedance measurements

$$L_{Mat} = \begin{bmatrix} 95.5 & 48.2 & 42 \\ 48.2 & 108 & 50.7 \\ 42 & 50.7 & 100 \end{bmatrix} \mu\text{H}$$

$$K_x = \begin{bmatrix} \cdot & 47.5 & 43 \\ 47.5 & \cdot & 48 \\ 43 & 48 & \cdot \end{bmatrix} \%$$

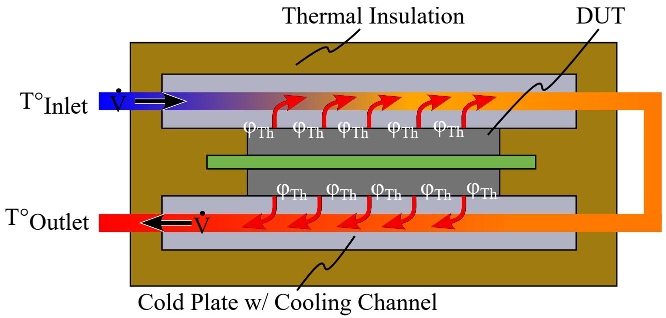

Figure 7. Graphical representation the double side cooling steady-calorimeter

3.1. Flow Calorimeter Set-Up

A schematic of the proposed steady-flow calorimeter is presented in the Figure 7. The losses are estimated by monitoring to the inlet/outlet temperatures (T_{In} ,T_{Out}), the flow rate ($\dot{V}$) and the coolant characteristics, being volumetric mass (ρ) and specific heat capacity (C_P) of water. The designed calorimeter mimics the final double side cooling system associated to the coupled inductors. A physical model can be defined thanks to the system geometry and the steady-state operation. Most of the heat is extracted by the cold plates. However, a lower part is transferred to the ambient air by the side insulation, by conduction through cables, and a small part from the cold plates directly to the air through the insulant. Therefore, the proposed model considers both heat transfer, to the coolant and to the air. For the latest, a proportional relationship is assumed based on the temperature difference between the ambient and the average coolant temperature, see equation 3 and 4.

$$\dot{Q}_{DUT} = \dot{Q}_{Coolant} + \dot{Q_{Air}} \tag{3}$$

$$\dot{Q}_{DUT} = \dot{V}\rho C_P(T_{Out} - T_{In}) + x\left(\frac{T_{Out} + T_{In}}{2} - T_{Amb}\right) \tag{4}$$

The ‘x’ coefficient is representative of the performances of the insulation, so the thermal leakage paths. This empirical corrective coefficient must be experimentally determined through a calibration procedure. This procedure consists in using the coupled inductors themself to generate DC losses. Those losses are measured by a power analyser (ZES ZIMMER LMG670), while the calorimeter is operational. The ‘x’ coefficient, and the uncertainty of the system, are determined by a proper data post-processing. In DC, the power analyser uncertainty within the 95 % confidence interval is obtained by considering individual voltage and current uncertainties. Indeed, one channel measures the voltage, while four channels are sharing the DC current, due to the max rated current being 32A, cf from equation 5 to equation 7 with V_{Max} and I_{Max} equal to 3V and 32A, respectively.

$$\delta V|_{95\%} = 0.02\% \cdot V_{Meas} + 0.08\% \cdot V_{Max} \tag{5}$$

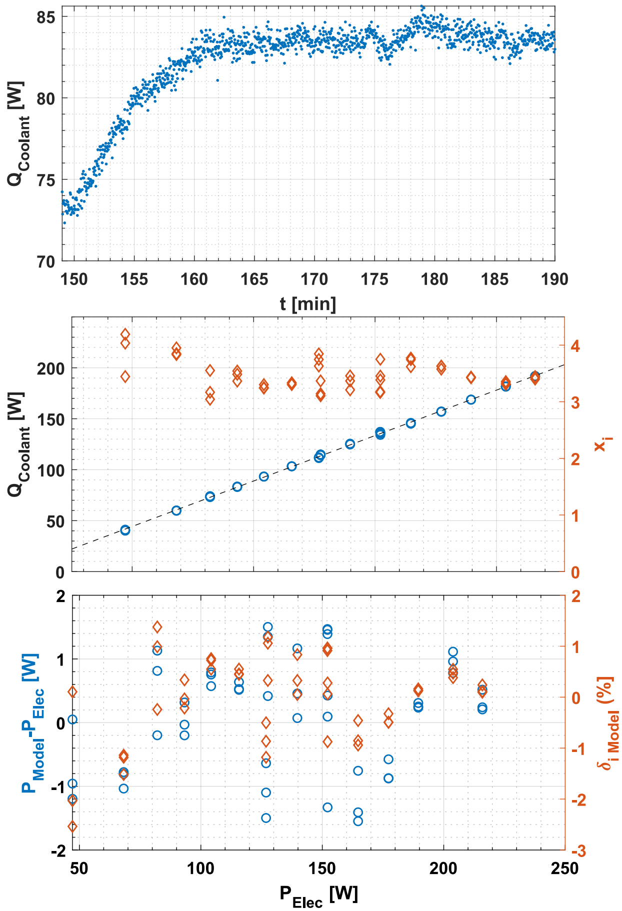

Figure 8. Calibration procedure’s experimental results. (Top) Instantaneous coolant heat transfer. (Centre) Comparison between losses extracted by the coolant and electrical power, and discrete estimation of ‘x’. (Bot) Power difference between losses estimated by the model considering $\bar{x}$ and the electrical power, and discrete model uncertainty.

$$\delta I_X|_{95\%} = 0.02\% \cdot I_{Meas} + 0.1\% \cdot I_{Max} \tag{6}$$

$$\delta P_{Elec} = \sqrt{\delta V^2 + 4\delta I_X{}^2} \tag{7}$$

The calibration is performed over a power range starting at 50 W up to 220 W, the flow rate is set to ~0.55 L/min for all the measurements. Each dataset, corresponding to a certain power level, are obtained after at least 30 min of operation. The measurement corresponding to one power level is repeated three times. The data ($\dot{V}$,T_{In} ,T_{Out}, T_{Amb}) selected for the calculation are the mean values of 200 successive instantaneous measurements, equivalent to 400 s of steady-state operation. The Figure 8 is presenting, the raw (no averaging) instantaneous power estimated with the calorimeter by only considering the heat transfer to the coolant (Top); the amount of losses transferred to the coolant versus the total electrical power measured by the LMG670, and the discrete ‘x’ values (Centre). Based on that, the average ‘x’ coefficient ($\bar{x}$=3.47) is applied within the model for the overall measurement range. The differences between the estimated losses from the model and the measured electrical power, see the Figure 8 (Bot), allow to calculate the overall system uncertainty, including the uncertainties from the flow-meter, temperature sensors and power analyser. Assuming a normal distribution, the maximal uncertainty within the 95% confidence interval is calculated based on the standard deviation (σ) of the model and the maximal uncertainty from the power analyser, see from equation 8 to equation 11.

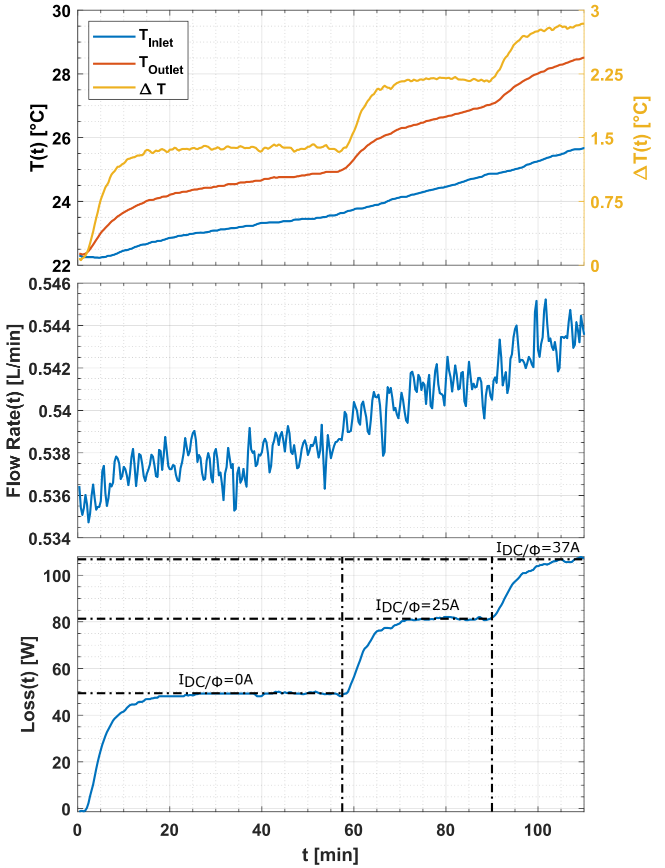

Figure 9. Loss measurement results using the Back-to-Back converters + the flow calorimeter set-up for three DC current values (0 A, 25 A/Φ & 37 A/Φ) corresponding to the no-load losses, half the nominal power losses and three-quarter of the nominal power losses at $V_{DC} = 700$ V and $V_{Out} = 350$ V.

$$\sigma_{Model} = \sqrt{\frac{1}{N-1}\sum_{i=1}^{N}(P_{i\,Model} - P_{i\,Elec})^2} \tag{8}$$

$$\sigma_{Elec} = \frac{max(\delta P_{Elec})}{2} \tag{9}$$

$$\sigma_{Sys} = \sqrt{\sigma_{Model}{}^2 + \sigma_{Elec}{}^2} \tag{10}$$

$$\delta_{Sys}|_{95\%} = 2 \cdot \sigma_{Sys} \tag{11}$$

From the experimental results, the standard deviation of the model and the power analyser are equal to 0.8759 W and 0.0705 W, respectively. Therefore, the overall system absolute uncertainty within the 95% confidence interval is equal to 0.8787 W, which corresponds to a maximal relative uncertainty of 1.755 % for a power level from 50 W up to 200 W. This calibration procedure allows to measure losses accurately and precisely by getting rid of systematic and random errors. Hereafter are presented the loss measurements under realistic operation conditions.

3.2. Coupled Inductors Loss Measurements

The loss measurements are presented in the Figure 9 from zero to 75 % of the nominal power, the Figure 10 presents the corresponding current waveforms. The measurements are consistent with the theoretical loss estimation. The difference between the theoretical and experimental HF loss values, 69 W and 50 W respectively, is certainly due to the temperature. Indeed, the device temperature considered in the optimisation is 100 °C, which is not the case of no-load operation. At a lower device temperature, the HF copper losses are reduced because of the copper thermal dependency characteristic while the core losses exhibit slightly higher losses. Nevertheless, based on the theoretical HF losses value and by adjusting the DC losses according to the operation point, 75 % of the nominal power, the estimated overall losses are equal to 104 W, while the measured losses are equal to 110 W, being only 6 % deviation. To accurately validate the optimisation procedure using the flow calorimeter, a proper temperature measurement, or estimation, within the prototype is definitely a key point, but quite difficult to set-up because of the electrical and magnetic constraints on the temperature sensor(s)[22].

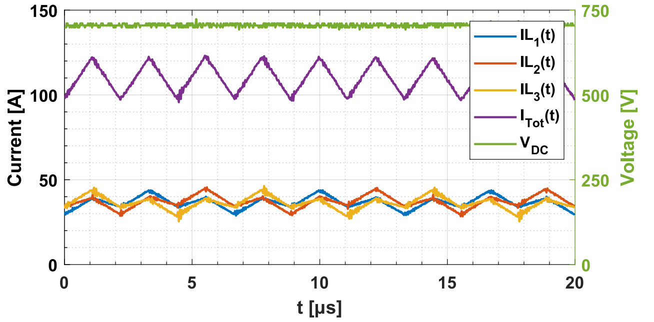

Figure 10. Current waveforms obtained during losses measurements at V_{DC} = 700 V, f_{SW} = 150 kHz and I_{DC}= 37 A

Finally, all the experimental results, small signal characterisation, saturation and losses evaluation, lend weight to the developed optimisation procedure, still with room for improvements, such as including of multi turns per layer capability to widen the design space, refinement of unbalanced DC currents to push forward the power density. Also confirming the interest of coupled magnetic components for high efficiency and higher power density required applications.

4. CONCLUSIONS

This paper presented the design and characterisation of PCB based 3-Φ coupled inductors made of two types of magnetic materials, iron powder and ferrite, aiming at increasing the power density of a PCB embedded IBC. The optimisation procedure based on FEA and analytical study have been introduced. The 2D FEA is particularly suitable for the investigated concept issued from PCB planar inductors, because of the form factor. The analytical procedure exploits the FEA data to quickly find an optimal design. For such a magnetic design, a particular attention must be paid to potential DC current unbalances. An underestimation of such phenomenon can quickly lead to the magnetic saturation. Even by considering this limiting factor, the selected optimal design was showing a substantial gain on the power density with magnetic cores being 40 % shorter than the unitary reference design.

The experimental assessment conducted onto the prototype show consistency with the optimisation procedure. To properly measure losses, a dedicated test-bench based on calorimetric method has been developed. As detailed, an appropriate calibration procedure contribute for getting results with good accuracy and precision, e.g ±1.755 %.

To conclude, this work highlighted the benefits of coupled magnetic components, even having asymmetrical coupling, on the design of high power density converter being constrained by DC magnetisation. This work will continue to further push the limits of this type of magnetic components.

5. REFERENCES

[1] Cyril Buttay, Christian Martin, Florent Morel, Remy Caillaud, Johan Le Lesle, Roberto Mrad, Nicolas Degrenne, and Stefan Mollov. Application of the PCB-Embedding Technology in Power Electronics-State of the Art and Proposed Development. *3D-PEIM 2018 - 2nd International Symposium on 3D Power Electronics Integration and Manufacturing*, 2018. 1

[2] Julien Morand, Rémi Perrin, Johan Le Leslé, and Guillaume Lefevre. Design and Evaluation of a Building Block for a 100 kW DC/DC Converter Based on PCB Process. In *CIPS 2022; 12th International Conference on Integrated Power Electronics Systems*, volume 2022-March, 2022. 1

[3] Johan Le Leslé, Guillaume Lefevre, Julien Morand, Rémi Perrin, Pierre Yves Pichon, and Guillaume Regnat. Characterisation of a Ferrite-Polymer Based Magnetic Material. *24th European Conference on Power Electronics and Applications, EPE 2022 ECCE Europe*, 2022. 1

[4] Magnetics Company. Magnetics Website. 1

[5] Chang Sung Corporation. Chang Sung Corporation Website. 1

[6] Panteleimon Papamanolis, Thomas Guillod, Florian Krismer, and Johann W. Kolar. Minimum Loss Operation and Optimal Design of High-Frequency Inductors for Defined Core and Litz Wire. *IEEE Open Journal of Power Electronics*, 1(August):469–487, 2020. 1

[7] Martin Pavlovsky, Giuseppe Guidi, and Atsuo Kawamura. Assessment of coupled and independent phase designs of interleaved multiphase buck/boost DC-DC converter for EV power train. *IEEE Transactions on Power Electronics*, 29(6):2693–2704, 2014. 1, 1

[8] Xinmin Liu, Zongheng Wu, Yiyang Yan, Yong Kang, and Cai Chen. A Novel Double-Sided Cooling Inverter Leg for High Power Density EV Based on Customized SiC Power Module. In *2020 IEEE Energy Conversion Congress and Exposition (ECCE)*, pages 3151–3154. IEEE, oct 2020. 1

[9] Ahmed H. Ismail, Zhuxuan Ma, Ahmad Al-Hmoud, and Yue Zhao. A High Frequency Coupled Inductor Design for High Power Density DC-DC Converters. *Conference Proceedings - IEEE Applied Power Electronics Conference and Exposition - APEC*, 2023-March:3275–3280, 2023. 1, 1

[10] P. Zumel, O. García, J. A. Cobos, and J. Uceda. Magnetic integration for interleaved converters. *Conference Proceedings - IEEE Applied Power Electronics Conference and Exposition - APEC*, 2(C):1143–1149, 2003. 1

[11] Charles R. Sullivan and Minjie Chen. Coupled Inductors for Fast-Response High-Density Power Delivery: Discrete and Integrated. In *2021 IEEE Custom Integrated Circuits Conference (CICC)*, pages 1–8. IEEE, apr 2021. 1

[12] Minjie Chen and Charles Sullivan. Unified Models for Coupled Inductors Applied to Multiphase PWM Converters. *IEEE Transactions on Power Electronics*, 36(12):14155–14174, 2021. 1

[13] Yu Chen Liu, Chen Chen, Yu Chen Chung, Meng Chi Tsai, and Katherine A. Kim. Integrated magnetics optimization process for an interleaved three-phase buck converter at 500 kHz. *IET Power Electronics*, (February):1–11, 2022. 1

[14] François Forest, Thierry A. Meynard, Jean Jacques Huselstein, Didier Flumian, Corentin Rizet, and Alain Lacarnoy. Design and characterization of an eight-phase-137-kW intercell transformer dedicated to multicell DC-DC stages in a modular UPS. *IEEE Transactions on Power Electronics*, 29(1):45–55, 2014. 1

[15] Eric Labouré, Alain Cuniére, T. A. Meynard, Francois Forest, and Emmanuel Sarraute. A theoretical approach to InterCell transformers, application to interleaved converters. *IEEE Transactions on Power Electronics*, 23(1):464–474, 2008. 1

[16] LI JIELI; SULLIVAN CHARLES R.; GENTCHEV ANGEL GENTCHEV. Method for making magnetic components with N-phase coupling, and related inductor structures, 2002. 1

[17] Youssef Elasser, Jaeil Baek, Charles R. Sullivan, and Minjie Chen. Modeling and design of vertical multiphase coupled inductors with inductance dual model. *Conference Proceedings - IEEE Applied Power Electronics Conference and Exposition - APEC*, pages 1717–1724, 2021. 1

[18] Georg Tobias Gotz, Alexander Stippich, Arne Hendrik Wienhausen, and Rik W. De Doncker. Design of Coupled Inductor for Two-Phase Synchronous Boost Converters in Automotive Applications. *Conference Proceedings - IEEE Applied Power Electronics Conference and Exposition - APEC*, 2020-March:2658–2665, 2020. 1

[19] Stefan Hoffmann and Eckart Hoene. Coupled PFC inductor for 22 kW on-board charger using PCB technology. *2023 25th European Conference on Power Electronics and Applications, EPE 2023 ECCE Europe*, pages 1–11, 2023. 1

[20] Yuliang Cao, Yijie Bai, Vladimir Mitrovic, Boran Fan, Dong Dong, Rolando Burgos, Dushan Boroyevich, Radha Krishna Moorthy, and Madhu Sudhan Chinthavali. 3.5 kW/in 3 Planar Coupled Inductor Design and Optimization for a 50 kW 3-level Four-Switch Buck-Boost (3L-FSBB) Converter. In *2022 IEEE Energy Conversion Congress and Exposition (ECCE)*, volume 2, pages 1–8. IEEE, oct 2022. 1

[21] Kapil Venkatachalam, Charles R. Sullivan, Tarek Abdallah, and Hernán Tacca. Accurate prediction of ferrite core loss with nonsinusoidal waveforms using only steinmetz parameters. *Proceedings of the IEEE Workshop on Computers in Power Electronics, COMPEL*, 2002-Janua(June):36–41, 2002. 2.1

[22] David Menzi, Garðar Eðvaldsson, Jonas E Huber, and Johann W Kolar. Core-as-a-Sensor: Ferrite DC-Resistance-Based Core Temperature Measurement of Magnetics. In *2023 IEEE Energy Conversion Congress and Exposition (ECCE)*, number Ecce, pages 6532–6534. IEEE, oct 2023. 3.2